Nonlinear signatures of Floquet band topology

Aleksandra Maluckov [![ORCID]],[1] Ekaterina Smolina,[2] Daniel Leykam [![ORCID]],[3] Sinan Gündoğdu [![ORCID]],[4,5]
Dimitris G. Angelakis,[3,6] and Daria A. Smirnova [![ORCID]][7,2]

[1]*Vinča Institute of Nuclear Sciences, University of Belgrade, National Institute of the Republic of Serbia, P.O.B. 522, 11001 Belgrade, Serbia*
[2]*Institute of Applied Physics, Russian Academy of Science, Nizhny Novgorod 603950, Russia*
[3]*Centre for Quantum Technologies, National University of Singapore, 3 Science Drive 2, 117543, Singapore*
[4]*Center for Theoretical Physics of Complex Systems, Institute for Basic Science, Daejeon 34126, Korea*
[5]*Department of Physics, Humboldt-Universität zu Berlin, Newtonstrasse 15, 12489 Berlin, Germany*
[6]*School of Electrical and Computer Engineering, Technical University of Crete, Chania 73100, Greece*
[7]*Nonlinear Physics Centre, Research School of Physics, Australian National University, Canberra ACT 2601, Australia*

We study how the nonlinear propagation dynamics of bulk states may be used to distinguish topological phases of slowly driven Floquet lattices. First, we show how instabilities of nonlinear Bloch waves may be used to populate Floquet bands and measure their Chern number via the emergence of nontrivial polarization textures in a similar manner to static (undriven) lattices. Second, we show how the nonlinear dynamics of nonstationary superposition states may be used to identify dynamical symmetry inversion points in the intracycle dynamics, thereby allowing anomalous Floquet phases to be distinguished from the trivial phase. The approaches may be readily implemented using light propagation in nonlinear waveguide arrays.

I. INTRODUCTION

Great progress and open challenges in the world of topological matter have provoked investigation of topological effects in periodically driven quantum systems. The particularities of driven systems allow a number of topological phenomena to occur, including quantized pumping and the existence of anomalous topological phases with no analog in undriven systems [1–6].

Topological phases of driven systems are classified according to the properties of their Floquet operators, i.e., the time-evolution operators describing the dynamics over one period of the drive [7,8]. Each eigenstate of the Floquet operator accumulates a phase ϕ over one driving period, giving the opportunity to define a quasienergy $\Omega = \phi/T$, the average phase accumulated per unit time. Being a phase variable, the quasienergy is periodic with period $2\pi/T$ and thus Floquet systems lack well-defined ground states. Nevertheless, they still support topological bulk-edge correspondences whereby the number of protected edge modes of finite systems is given by topological invariants of the bulk Floquet eigenstates [4–6].

Photonics provide a highly flexible platform for implementing periodically driven systems and observing their topological properties [9,10]. For example, in optical waveguide arrays, the longitudinal propagation distance plays the role of time, allowing Floquet phenomena to be realized using purely spatial modulation of the refractive index [11–16].

Nonlinear effects are now being considered in the context of topological photonic systems [17], opening opportunities for measurement and manipulation of topological bands and giving rise to unique classes of self-localized nonlinear modes

[18–20]. For example, bulk and edge solitons have been experimentally observed using two-dimensional Floquet waveguide lattices [21–24]. These recent studies motivate interest in how nonlinearity may be used to probe bulk topological invariants of Floquet systems.

Recently, we showed how the bulk topological invariants of two-dimensional undriven lattices can be measured using nonlinear modulational instability of bulk Bloch waves [25]. Modulational instability is the process by which an initially uniform Bloch (or plane) wave becomes strongly inhomogeneous via the amplification of small perturbations, leading to excitation of other Bloch waves [26,27]. In this case, the source of the gain is nonlinear wave mixing seeded by the high intensity Bloch wave. The approach of Ref. [25] relied on one key property of modulational instability: its relatively narrow gain bandwidth, meaning that for sufficiently low light intensities only Bloch waves belonging to the same band will be amplified. Thus, the modulational instability converts a single Bloch wave initial state to a mixture of all the Bloch waves comprising an energy band of the lattice. Once this conversion has occurred, measurements of the wave field in Fourier space can be used to determine the spin or polarization structure of the band's Bloch waves, from which topological invariants such as their Chern number can be readily computed [28].

The purpose of this paper is to establish how the predictions of our earlier study Ref. [25] may be applied to nonlinear Floquet topological systems such as optical waveguide arrays. These systems can be well-described by effective static Hamiltonians in the case of high-frequency modulation; in this limit, the results of Ref. [25] are directly applicable. Therefore, the focus of this paper is the behavior in the

low-frequency driving regime, which, in particular, can lead to the emergence of anomalous Floquet topological phases.

To this end, we analyze modulational instability in a stroboscopically driven nonlinear square lattice model. Each periodic drive cycle is divided into four steps. During each step, pairs of neighboring waveguides are coupled. By tuning the coupling strength during each step, different topological phases hosting protected edge or corner modes can be realized, including the trivial insulator (TI), Chern insulator (CI), anomalous Floquet insulator (AFI), and anomalous Floquet higher order topological insulator (AFHOTI) [29]. Similar to static lattices, transitions between distinct topological phases require the gap between the two bulk Floquet bands to close.

We show using numerical simulations of the governing nonlinear Schrödinger equation how the modulational instability dynamics can identify CI phases using the field polarization measures considered in Refs. [25,28]. These measures, however, cannot distinguish anomalous Floquet phases from the TI phases, which requires knowledge of the full time evolution within one driving period. To address this limitation, we consider the nonlinear dynamics of nonstationary plane wavelike states formed by equal superpositions of both bands of the considered Floquet lattice. We show that the nonlinear dynamics can be used to track the Floquet bands' symmetry eigenvalues at the high-symmetry Brillouin zone points and thereby distinguish the anomalous Floquet phases from the trivial phase [29].

The outline of the paper is as follows: The model equations and band structures of Floquet systems are considered in Sec. II. The modulation instability (MI) is investigated in Sec. III, where we demonstrate the ability of MI to generate a quasisteady state with a well-defined polarization field. Next, in Sec. IV we show how the dynamics of superposition states may be used to identify anomalous Floquet phases. Section V concludes.

II. FLOQUET LATTICE MODEL

We consider nonlinear light propagation in the periodically driven bipartite square lattice model of Ref. [29], shown in Fig. 1(a). Previous studies have considered similar models [4,12,14,15,20,29,30]. The propagation dynamics are described by the nonlinear Schrödinger equation

$$i\partial_z |\psi(\mathbf{r}, z)\rangle = [\hat{H}_L(z) + \hat{H}_{NL}(\psi)] |\psi(\mathbf{r}, z)\rangle, \quad (1)$$

where the wave field $|\psi(\mathbf{r}, z)\rangle = [a(\mathbf{r}), b(\mathbf{r})]^T$ (omitting z arguments for brevity) encodes the optical field amplitude on the two sublattices, $\hat{H}_L(z)$ is the periodically modulated linear tight-binding Hamiltonian, and the propagation distance z is analogous to time. For convenience, we will use z and time interchangeably in the following.

$\hat{H}_{NL}(\psi) = g\, \mathrm{diag}[f(|a(\mathbf{r})|^2), f(|b(\mathbf{r})|^2)]$ describes the on-site nonlinearity with strength g, which is a function of the local intensity at each lattice site. For linear stability analysis, we consider pure Kerr nonlinearity $f(I) = I$, while for the beam propagation simulations we use saturable nonlinearity $f(I) = I/(1 + I)$, which serves to model effects such as multiphoton absorption and material damage, which limit the practical strength of the Kerr effect [27]. The saturable
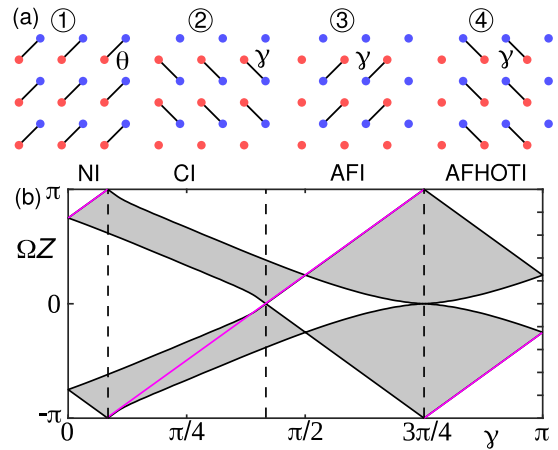

FIG. 1. (a) Schematic of one driving period, consisting of each nonlinear site being coupled to its neighbors in turn with strength $J_1 = \theta$, $J_{2-4} = \gamma$ for a duration $l = 1$. (b) Linear Floquet-Bloch band structure as a function of γ for fixed $\theta = 3\pi/4$. The purple line indicates the quasienergy of the symmetric Bloch wave with momentum $\mathbf{k} = 0$. Dashed lines denote boundaries between different topological phases (normal insulator NI, Chern insulator CI, anomalous Floquet insulator AFI, and anomalous Floquet higher order topological insultor AFHOTI).

nonlinearity reduces to Kerr nonlinearity in the low intensity limit.

A. Linear Floquet spectrum

We now introduce and briefly review the properties of the linear lattice model ($g = 0$). As $\hat{H}_L(z)$ is a periodically modulated lattice Hamiltonian, it gives rise to Floquet-Bloch modes $|u_n(\mathbf{k})\rangle e^{i\mathbf{k}\cdot\mathbf{r}}$ with wave number $\mathbf{k}$, which are invariant (up to a phase factor) under spatial translations by a lattice vector and after one period of the modulation, i.e.,

$$\hat{U}_L(\mathbf{k}, Z) |u_n(\mathbf{k})\rangle = \exp\left(-i\int_0^Z \hat{H}_L(\mathbf{k}, z)dz\right) |u_n(\mathbf{k})\rangle$$
$$= \lambda_n(\mathbf{k}) |u_n(\mathbf{k})\rangle, \quad (2)$$

where $\hat{U}_L(\mathbf{k})$ is the linear Floquet evolution operator, whose eigenvalues $\lambda_n(\mathbf{k})$ forms a discrete set of bands indexed by n. The Floquet evolution operator can be used to define a static effective Floquet Hamiltonian $\hat{H}_F$ via $\hat{U}_L(\mathbf{k}, Z) = \exp(-iZ\hat{H}_F(\mathbf{k}))$ analogous to Hamiltonians of nondriven lattices, with bands of quasienergy eigenvalues Ω_n defined modulo $2\pi/Z$:

$$\Omega_n(\mathbf{k}) = \frac{i}{Z} \ln \lambda_n(\mathbf{k}). \quad (3)$$

During each period Z of the Floquet modulation, each site is coupled one at a time to each of its four nearest neighbours with strength J_j, described by the Bloch Hamiltonian

$$\hat{H}_L(\mathbf{k}, z) = \sum_{j=1}^4 \begin{pmatrix} 0 & J_j(z)e^{i\mathbf{k}\cdot\boldsymbol{\delta}_i} \\ J_j(z)e^{-i\mathbf{k}\cdot\boldsymbol{\delta}_i} & 0 \end{pmatrix}, \quad (4)$$

where $\boldsymbol{\delta}_1 = (\frac{1}{2}, \frac{1}{2})$, $\boldsymbol{\delta}_2 = (\frac{1}{2}, -\frac{1}{2})$, $\boldsymbol{\delta}_3 = -\boldsymbol{\delta}_1$, and $\boldsymbol{\delta}_4 = -\boldsymbol{\delta}_2$ are displacements between neighboring sites. We normalize

the lattice period to $Z = 4$, and set $J_1(z) = \theta$, $J_2(z) = J_3(z) = J_4(z) = \gamma$ when the two neighbors are coupled, and zero otherwise [29].

The evolution operator can be written as

$$\hat{U}_L(\boldsymbol{k}) = \hat{S}_\gamma(-\kappa_-)\hat{S}_\gamma(-\kappa_+)\hat{S}_\gamma(\kappa_-)\hat{S}_\theta(\kappa_+), \qquad (5)$$

where $\kappa_+ = \boldsymbol{\delta}_1 \cdot \boldsymbol{k}$, $\kappa_- = \boldsymbol{\delta}_2 \cdot \boldsymbol{k}$, and

$$\hat{S}_J(\kappa) = \begin{pmatrix} \cos J & -ie^{i\kappa}\sin J \\ -ie^{-i\kappa}\sin J & \cos J \end{pmatrix}. \qquad (6)$$

Owing to our normalization of the coupling length to $Z/4 = 1$, $\hat{S}_J(\kappa)$ only depends on J modulo 2π, therefore we will use coupling strength and coupling angle interchangeably.

The quasienergy band structure as a function of γ for fixed $\theta = 3\pi/4$ is plotted in Fig. 1(b). Owing to the bipartite Hamiltonian which obeys particle-hole symmetry [29], two quasienergy gaps occur: around $\Omega = 0$ and $\Omega = \pi/Z$. Each gap may host topological edge or corner modes. The gap closes at boundaries between distinct topological phases, corresponding to Dirac points in the bulk band structure.

The multiple crossing points in Fig. 1(b) indicate that several topological phases can be realized by tuning the single parameter γ: a NI phase in which none of the gaps support any topological edge or corner modes; a CI phase, in which only one gap hosts chiral edge modes; an anomalous Floquet topological insulator phase, in which both gaps host chiral edge modes, and an AFHOTI phase, in which both gaps host topological corner modes.

The first Dirac point $\gamma = \pi/12$ corresponds to $\lambda_{1,2} = -1$ and divides the NI and CI phases. The second Dirac point $\gamma = 5\pi/12$ corresponds to $\lambda_{1,2} = 1$ and divides the CI and AFI phases, while the third Dirac point at $\gamma = 3\pi/4$ and $\lambda_{1,2} = -1$ separates AFI and AFHOTI phases. In addition, there are other critical points at $\gamma = 0, \pi/2$, and π, corresponding to purely flat quasienergy bands with eigenvalues independent of momentum $\boldsymbol{k}$.

B. Topological invariants

The presence of distinct quasienergy bands allows topological invariants originally derived for static systems to describe the stroboscopic dynamics of Floquet systems. For example, the CI phase can be identified by integrating the Berry curvature of the Bloch wave eigenstates over the Brillouin zone to obtain the Chern number of the nth band [9,10]:

$$C_n = \frac{i}{2\pi}\int_{\text{BZ}} \left[\langle\partial_{k_x}u_n|\partial_{k_y}u_n\rangle - \langle\partial_{k_y}u_n|\partial_{k_x}u_n\rangle\right]d^2\boldsymbol{k}. \qquad (7)$$

The Chern number has a variety of interpretations and physical implications. For example, C_n counts the difference between the number of chiral edge states emerging from the top and bottom of the nth band of a semi-infinite lattice.

In the following, we will make use of the relation between the Chern number and polarization textures of the Bloch functions [28]. Specifically, one can construct a polarization field $\boldsymbol{s}(\boldsymbol{k}) = \langle u_n(\boldsymbol{k})|\hat{\boldsymbol{\sigma}}|u_n(\boldsymbol{k})\rangle$ by projecting the Bloch functions $|u_n(\boldsymbol{k})\rangle$ onto any two linearly independent polarization (or spin) directions. In our case, $\hat{\boldsymbol{\sigma}} = (\hat{\sigma}_x, \hat{\sigma}_y, \hat{\sigma}_z)$ are Pauli
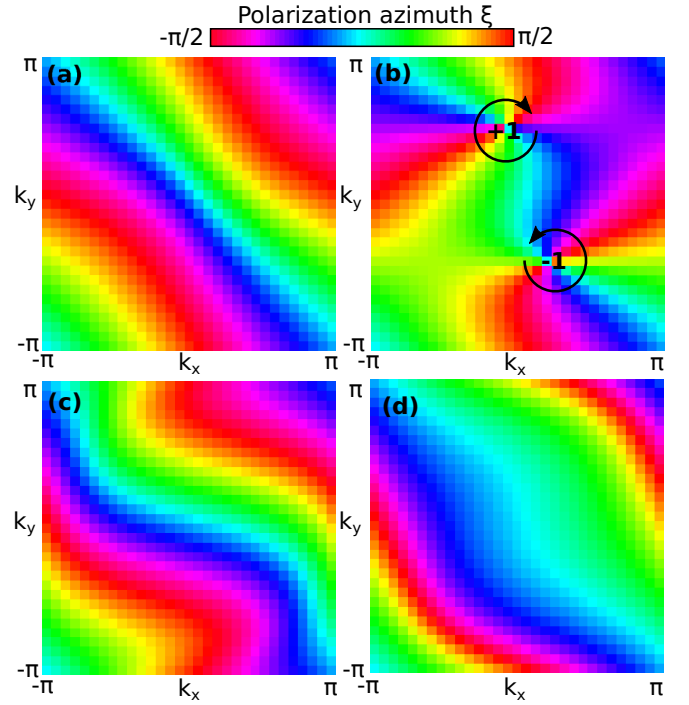

FIG. 2. Polarization textures $\xi(\boldsymbol{k})$ of the Bloch functions eigenstates of Eq. (4) obtained using Eqs. (8)–(11). (a) Trivial phase ($\gamma = \pi/24$). (b) Chern insulator phase ($\gamma = \pi/6$). ± 1 denotes the sign of the polarization ellipticity at the vortex cores. (c) Anomalous Floquet insulator phase ($\gamma = 7\pi/12$). (d) Anomalous Floquet higher order topological insulator phase ($\gamma = 11\pi/12$).

matrices acting on the sublattice degree of freedom, such that

$$s_x(\boldsymbol{k}) = 2\text{Re}[a(\boldsymbol{k})^*b(\boldsymbol{k})]/(|a(\boldsymbol{k})|^2 + |b(\boldsymbol{k})|^2), \qquad (8)$$

$$s_y(\boldsymbol{k}) = 2\text{Im}[a(\boldsymbol{k})^*b(\boldsymbol{k})]/(|a(\boldsymbol{k})|^2 + |b(\boldsymbol{k})|^2), \qquad (9)$$

$$s_z(\boldsymbol{k}) = (|a(\boldsymbol{k})|^2 - |b(\boldsymbol{k})|^2)/(|a(\boldsymbol{k})|^2 + |b(\boldsymbol{k})|^2). \qquad (10)$$

Geometrically, the vector field $\boldsymbol{s}(\boldsymbol{k})$ can be parameterized in terms of a polarization azimuth $\xi(\boldsymbol{k})$ and ellipticity $\chi(\boldsymbol{k})$, which are related to the sublattice amplitudes via [28]

$$\xi(\boldsymbol{k}) = \tfrac{1}{2}\tan^{-1}(s_y/s_x), \quad \chi(\boldsymbol{k}) = \tfrac{1}{2}\sin^{-1}(s_z). \qquad (11)$$

Provided $s^2 = \boldsymbol{s}\cdot\boldsymbol{s} > 0$ over the entire Brillouin zone, the polarization state is well-defined for all $\boldsymbol{k}$ and is sensitive to the Chern number Eq. (7). To be precise, the Chern number is obtained as a sum of the phase singularities of the polarization azimuth ξ weighted by $\text{sgn}(\chi)$ at the singularity [28]. The Chern number computed using the polarization state is quantized and cannot change unless the polarization becomes undefined at some wave vector $\boldsymbol{k}_c$ at which the band gap closes, i.e., $s^2(\boldsymbol{k}_c) = 0$.

Figure 2 illustrates the polarization textures of the Bloch functions in each of the four phases of Eq. (4) at $z = Z$. Polarization vortices are only useful for identifying the CI phase and cannot distinguish the anomalous Floquet phases from the trivial phase.

The anomalous Floquet phases emerge due to the periodicity of the quasienergy eigenvalues, which leads to topological phenomena inaccessible in static systems. Since the quasienergies are only defined modulo $2\pi/Z$, it is possible for chiral edge states to traverse all of the band gaps, including what would be the semi-infinite gaps of a static system, corresponding to an AFI phase with vanishing Chern number. The topological invariants describing anomalous Floquet phases cannot be obtained using just $\hat{H}_F$ or $\hat{U}_L(Z)$, but instead require analysis of the full evolution throughout one driving period [7,8],

$$\hat{U}(z) = \mathcal{T} \exp\left(-i\int_0^z H(z')dz'\right), \qquad (12)$$

where $\mathcal{T}$ denotes time ordering. For example, the anomalous Floquet topological insulator phase is identified by the winding number [4]

$$W = \frac{1}{8\pi^2}\int_0^Z dz \int_{\mathrm{BZ}} d^2\boldsymbol{k}\,\mathrm{Tr}\big(\hat{U}^{-1}\partial_z\hat{U}\big[\hat{U}^{-1}\partial_{k_x}\hat{U}, \hat{U}^{-1}\partial_{k_y}\hat{U}\big]\big). \qquad (13)$$

The intraperiod evolution operator $\hat{U}(z)$ is generally not periodic in time, despite the Hamiltonian obeying $\hat{H}_L(z+Z) = \hat{H}_L(z)$. For bulk systems, the family of Bloch evolution operators $\hat{U}(\boldsymbol{k}, z)$ acting within the space of periodic Bloch functions can be written in the form

$$\hat{U}(\boldsymbol{k}, z) = \sum_{n=1}^N \hat{P}_n(\boldsymbol{k}, z)\, \exp(-i\varphi_n(\boldsymbol{k}, z)), \qquad (14)$$

where $\hat{P}_n$ is the projector onto the nth eigenstate of $\hat{U}(\boldsymbol{k}, z)$, $\exp(-i\varphi_n(\boldsymbol{k}, z))$ the corresponding eigenvalues, and $\varphi_n(\boldsymbol{k}, z)$ are called the phase bands of the system [31,32]. The phase bands depend on time and at $z = Z$ they are identical to the Floquet bands, i.e., the quasienergies. Anomalous Floquet phases may be identified by band crossings of the phase bands, indicating that the system cannot be adiabatically deformed into a static (undriven) system.

Figure 3 illustrates the phase band spectrum of the system for various γ. It is predicted and clearly seen in the corresponding phase band representation, that the phase band spectrum of the anomalous Floquet phases, in contrast to the NI and CI phases, hosts multiple degeneracies within the driving period. As degeneracies within a three-dimensional parameter space (k_x, k_y, z) are topologically protected, small changes in the lattice parameters can shift the positions of the degeneracies but not remove them. The presence of multiple phase band degeneracies also means that the system cannot be adiabatically (without band crossing) transformed to an undriven system [31]. When viewing the lattice stroboscopically, i.e., only considering the quasienergy bands, these degeneracies are hidden.

Recently, Ref. [29] developed an alternative to Eq. (13) for obtaining bulk topological properties of the anomalous Floquet phases of driven lattices with chiral symmetry. Thanks to the chiral symmetry, it suffices to study the properties of the eigenstates at the high-symmetry points of the Brillouin zone to distinguish the different phases. At the high-symmetry points, $[H(z), H(z')] = 0$ for all z, z'. Therefore, the eigenstates of the phase operator $\hat{U}(z)$ are independent of z; all that changes are their eigenvalues. The number and position
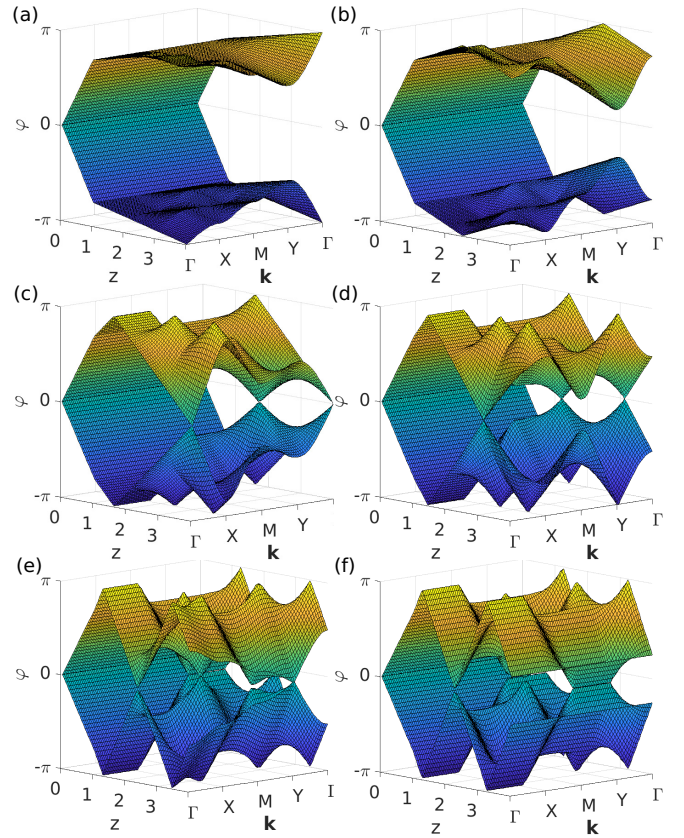

FIG. 3. Phase band profiles along high-symmetry lines in the Brillouin zone for $\theta = 3\pi/4$ and (a) $\gamma = \pi/12$ (the first Dirac point), (b) $\gamma = \pi/6$ (Chern insulator phase), (c) $\gamma = 5\pi/12$ (the second Dirac point), (d) $\gamma = 7\pi/12$ (anomalous Floquet insulator phase), (e) $\gamma = 11\pi/12$ (anomalous Floquet higher order topological insulator phase), and (f) $\gamma = \pi$ (flat-band limit). Unremovable phase band crossings occur within the modulation cycle in the anomalous Floquet phases.

(quasienergy 0 or π) of the band crossings of $\hat{U}(z)$ at the high-symmetry points can be used to distinguish trivial, CI, and anomalous Floquet topological phases.

The inversion symmetry eigenvalues calculated with inversion symmetry operator $\hat{\sigma}_x$ for the lower-band Floquet eigenstate at the high-symmetry points of the Brillouin zone are shown in Fig. 4, top row. The different signs at Γ and M in the CI phase indicates the nonzero Chern number. To capture a difference between NI, AFI, and AFHOTI, all possessing the vanishing Chern number, we have to inspect the microscopic dynamics within one period. In contrast to the NI phase, AFI and AFHOTI phases exhibit many dynamical symmetry inversion points, see Fig. 4. In their neighborhood, the effective Hamiltonian $\hat{H}_{\mathrm{eff}}(\boldsymbol{k}_0, z)$ appearing in the evolution operator $\hat{U}(\boldsymbol{k}_0, z) = e^{-i\hat{H}_{\mathrm{eff}}(\boldsymbol{k}_0, z)}$ with the momentum $\boldsymbol{k}_0$ can be defined as

$$\hat{H}_{\mathrm{eff}}(\boldsymbol{k}_0, z_m + \Delta z_m) = \varphi_0(\boldsymbol{k}_0, z_m) + S(\boldsymbol{k}_0, z_m)\gamma\,\Delta z_m\hat{\sigma}_x, \quad (15)$$

whose sign characteristics $S(\boldsymbol{k}_0, z_m)$ are listed in Table I. In the AFI phase, there are two stable crossing points at Γ for the 0 and π gaps. In the AFHOTI phase, we observe three stable crossing points at Γ. Three crossing points at M all appear
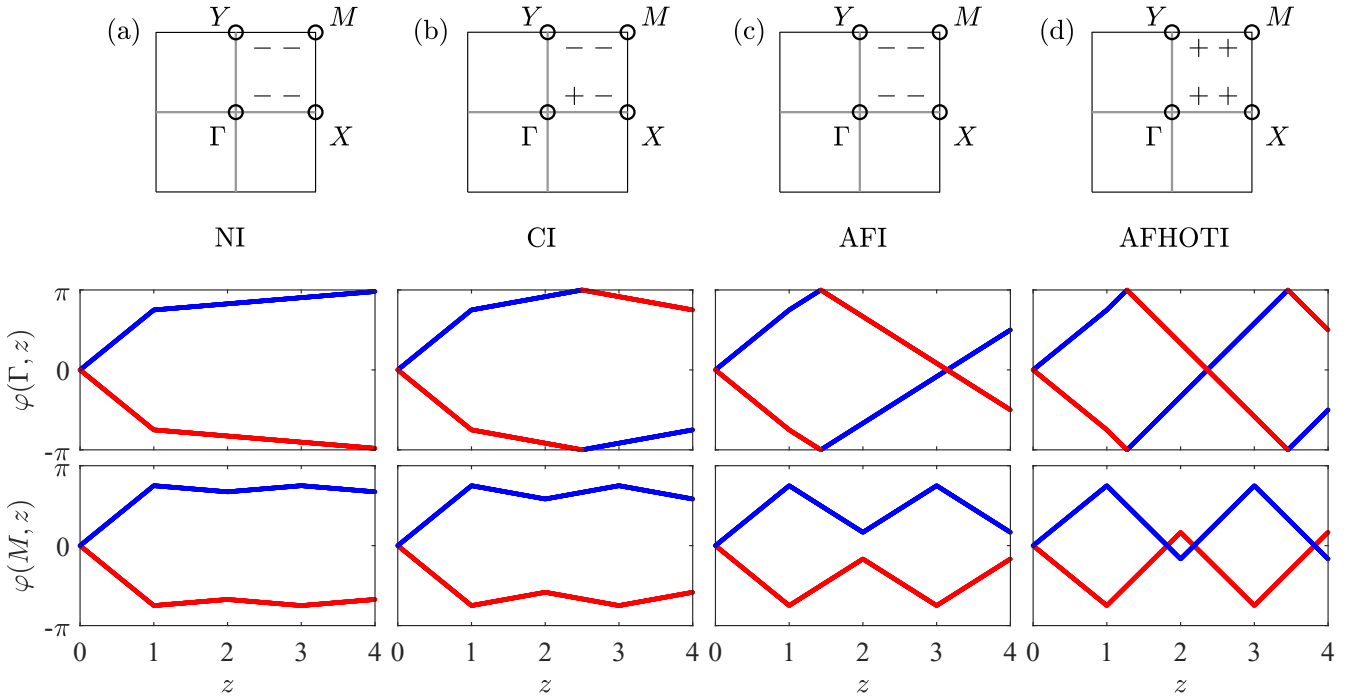
FIG. 4. Inversion symmetry eigenvalues calculated for the lower-band Floquet eigenstate at the high-symmetry momentum points of the Brillouin zone (top row) and phase bands (middle and bottom rows) at fixed $\theta = 3\pi/4$ for different topological phases: (a) $\gamma = \pi/13$ (NI), (b) $\gamma = \pi/6$ (CI), (c) $\gamma = 7\pi/12$ (AFI), (d) $\gamma = 11\pi/12$ (AFHOTI). Phase bands in the high-symmetry directions Γ and M are plotted over one period. The inversion symmetry eigenvalues for red (blue) bands are -1 $(+1)$.

for the 0 gap and counts as one, since two of the points with opposite S can annihilate with each other. An odd number of stable crossing points would hint to the first-order topological phase. However, in our case, the system supports an even number of stable crossing points and such symmetry analysis cannot unambiguously distinguish between the first-order and higher-order topological phases.

III. MODULATIONAL INSTABILITY AND DYNAMICS

Now we consider the properties of the full nonlinear evolution Eq. (1). The linear Floquet modes may persist as nonlinear Floquet modes, solutions of the nonlinear eigenvalue problem

$$|u_{NL}(z + Z)\rangle = \hat{U}_{NL} |u_{NL}(z)\rangle$$

$$= \exp\left(-i \int_0^Z [\hat{H}_L(z) + \hat{H}_{NL}]dz\right) |u_{NL}\rangle$$

$$= e^{-iZ\Omega_{NL}} |u_{NL}(z)\rangle. \quad (16)$$

TABLE I. Sign characteristics $S(\boldsymbol{k}_0, z_m)$ of the effective continuum Hamiltonian near dynamical symmetry inversion point z_m in the high-symmetry directions $\boldsymbol{k}_0 = (0, 0)$ and $\boldsymbol{k}_0 = (\pi, \pi)$ labeled with Γ and M, respectively.

Phase	NI		CI		AFI		AFHOTI	
Point	Γ	M	Γ	M	Γ	M	Γ	M
$\varphi_0(\boldsymbol{k}_0, z_m) = \pi$	0	0	+	0	+	0	++	0
$\varphi_0(\boldsymbol{k}_0, z_m) = 0$	0	0	0	0	+	0	+	(−+)−

As each step of the modulation cycle forms a nonlinear Schrödinger dimer, which is integrable, the dynamics are, in principle, analytically solvable. However, the solution will take a highly complicated form as the analytical solution of the dimer for arbitrary initial conditions involves elliptic functions [33]. Alternatively, Eq. (16) can be solved numerically using the self-consistency method (see, e.g., Refs. [18,20]).

In the following, we will restrict our analysis to the simplest nonlinear Bloch wave solutions, those at the high-symmetry Brillouin zone points $\boldsymbol{k}_0$ (see Table II), which have modal profiles $|u_{NL}^{\pm}(\boldsymbol{k}_0)\rangle = (\pm e^{i\Theta(\boldsymbol{k}_0)}, 1)^T/\sqrt{2}$, independent of θ, γ, and g, with unitary total intensity. Term $\Theta(\boldsymbol{k}_0)$ denotes the corresponding nonlinear mode phase. The normalized states $|u_\pm\rangle = (\pm 1, 1)^T/\sqrt{2}$ at Γ point have a simple wave profile since no complex phase or intensity modulation is required, making these states more easily accessible in experiments [21–23].

TABLE II. Characteristics of the eigenstates at the high-symmetry points. ω_j are linear eigenvalues of of $\hat{H}_L$ for the selected eigenvector at each quarter of the period. Eigenenergies of $\hat{H}_L$ are $\omega_j = \pm J_j$, and normalised eigenmodes are $|u_j(\boldsymbol{k}_0)\rangle = (\pm e^{i\boldsymbol{k}_0 \cdot \boldsymbol{\delta}_j}, 1)^T/\sqrt{2}$.

Point	$\boldsymbol{k}_0$	Eigenvalue	Eigenmode	ω_1	ω_2	ω_3	ω_4
Γ	(0,0)	$e^{-i(3\gamma+\theta)}$	$(1, 1)^T/\sqrt{2}$	θ	γ	γ	γ
M	(π, π)	$e^{-i(\gamma-\theta)}$	$(1, 1)^T/\sqrt{2}$	$-\theta$	γ	$-\gamma$	γ
X	$(\pi, 0)$	$e^{i(\gamma-\theta)}$	$(i, 1)^T/\sqrt{2}$	θ	γ	$-\gamma$	$-\gamma$
Y	$(0,\pi)$	$e^{i(\gamma-\theta)}$	$(i, 1)^T/\sqrt{2}$	θ	$-\gamma$	$-\gamma$	γ

There is no energy transfer between the sublattices and the Kerr nonlinear terms are independent of z, such that $\hat{H}_{NL} = g\hat{1}$, which commutes with $\hat{H}_L(z)$. Hence the nonlinear Bloch waves' quasienergies are $\Omega_{NL} = \Omega/Z + g/2$. Note that even if g is small, the relative strength of the nonlinearity can be made increased by lengthening the modulation period Z. Because $\hat{H}_{NL}$ commutes with $\hat{H}_L$, these nonlinear Bloch wave eigenvectors are independent of Z.

We are interested in understanding how the features of the linear Floquet spectrum (e.g., dispersion, topological properties) are imprinted in the nonlinear Bloch waves' stability. Since $\hat{H}$ is invariant under the staggering transform, $(a_r, b_r)^T \rightarrow (-a_r, b_r)^T$, $z \rightarrow -z$, $g \rightarrow -g$, it is sufficient to consider only the symmetric Bloch waves $|u_+\rangle = (1, 1)^T/\sqrt{2}$.

A. Linear stability analysis

To enlighten the MI development in the Floquet lattice, we study the stability properties of the nonlinear Bloch waves. Consider a small perturbation to a nonlinear Bloch wave, $|\psi_r(z)\rangle = (|u_{NL}^+(\mathbf{k}_0)\rangle + |\delta\psi_r\rangle)e^{-i(\omega_j + g/2)z}e^{i\mathbf{k}_0 \cdot \mathbf{r}}$, where $(\omega_j + g/2)$ is the nonlinear mode's instantaneous energy at step j of the modulation and $\mathbf{k}_0$ is the wave vector in the vicinity of which we investigate the instability.

We substitute this state into the evolution Eq. (1) for each of the modulation steps, retaining only the linear terms of the perturbation. To perform the linear stability analysis, we make use of the identities $\hat{k} = -i\partial_r$: $e^{i\hat{k}\delta_n} = \sum_n \frac{(i\hat{k}\delta_n)^n}{n!} = \sum_n \frac{(\partial_r \delta_n)^n}{n!}$, $e^{i\hat{k}\delta_n}[e^{ikr}] = e^{ik\delta_n}e^{ikr}$.

Considering perturbations of the form $|\delta\psi_r\rangle = |v_p\rangle e^{i\mathbf{p}\cdot\mathbf{r}} + |w_p^*\rangle e^{-i\mathbf{p}\cdot\mathbf{r}}$ and applying the standard linear stability analysis, the Hamiltonian-like operator governing the evolution of the perturbation vector $(v, w, v^*, w^*)^T$ at each step of the driving period takes the form

$$\hat{H}'_j = \begin{pmatrix} g - \omega_j & J_j e^{i\mathbf{p}\cdot\delta_j} e^{i\mathbf{k}_0\cdot\delta_j} & \frac{1}{2}ge^{2i\Theta(\mathbf{k}_0)} & 0 \\ J_j e^{-i\mathbf{p}\cdot\delta_j} e^{-i\mathbf{k}_0\delta_j} & g - \omega_j & 0 & \frac{1}{2}ge^{2i\Theta(\mathbf{k}_0)} \\ -\frac{1}{2}ge^{-2i\Theta(\mathbf{k}_0)} & 0 & \omega_j - g & -J_j e^{i\mathbf{p}\cdot\delta_j} e^{-i\mathbf{k}_0\cdot\delta_j} \\ 0 & -\frac{1}{2}ge^{-2i\Theta(\mathbf{k}_0)} & -J_j e^{-i\mathbf{p}\cdot\delta_j} e^{i\mathbf{k}_0\cdot\delta_j} & \omega_j - g^2 \end{pmatrix}, \tag{17}$$

where $\omega_j = \pm J_j$ depends on the chosen mode (see Table II).

Using these Hamiltonians, we may construct the evolution operator for perturbations in the nonlinear case as $\tilde{U} = e^{-i\hat{H}'_1}e^{-i\hat{H}'_2}e^{-i\hat{H}'_3}e^{-i\hat{H}'_4}$. If any eigenvalues $\tilde{\lambda}$ of $\tilde{U}$ have modulus $|\tilde{\lambda}| > 1$, the nonlinear Bloch wave is unstable.

The eigenvalues of $\tilde{H}_{1,4}$ are $0, 0, \pm 2\sqrt{J_{1,4}(J_{1,4} - g)}$. Thus, a sufficient condition for instability is for one of the nonlinear couplers to be unstable, i.e., when $g > J_{1-4}$ ($J_1 = \theta$, $J_{2-4} = \gamma$). This condition is independent of the lattice's band structure, and so less interesting from our point of view. Therefore, we focus our attention to $g < J$ (i.e., γ and θ). This is also the more practical case to consider, given the weakness of the Kerr nonlinear effect.

The numerically obtained instability rates for the high-symmetry points are shown in Fig. 5 as a function of γ and g. For weak nonlinearity, the stability windows are dictated by the quasienergy of the linear Bloch wave. When the quasienergy lies at an upper (lower) band edge, instability will occur for weak positive (negative) g. Otherwise, the nonlinearity needs to be sufficiently strong to shift the quasienergy into a band gap for instabilities to occur.

At the critical points of the band structure, i.e., the Dirac points and flat-band limits, the sign of the wave effective mass flips, resulting in (for fixed g) transitions between stability and instability. These transitions can be seen for the Γ and M point Bloch waves, which lie at band edges. On the other hand, the X and Y points are typically saddles of the quasienergy bands, meaning that sufficiently large nonlinearity is always required for the instability to develop.

This behavior of the linear stability eigenvalues closely resembles that of the Bloch waves of undriven lattices [25], despite the modulation frequency being low and the presence of anomalous Floquet phases. The linear perturbation

spectrum exhibits stable lines corresponding to nonlinearity-induced band inversions. These transitions correspond to the instability eigenvalues becoming complex, i.e., the dominant instability changes from real to oscillatory. This can be understood in terms of the nonlinearity reducing the amount of
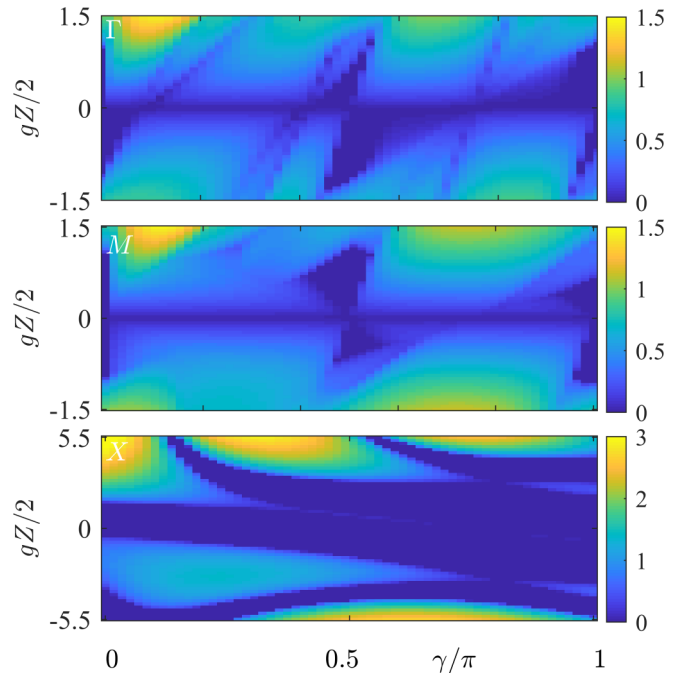

FIG. 5. The maximum values of the instability growth rate $\max(\ln|\lambda|)Z$ as a function of the coupling parameter γ and nonlinearity strength g for fixed $\theta = 3\pi/4$ at each of the high-symmetry points of the Brillouin zone, labeled with Γ, M, X.

energy transferred to the neighboring waveguide during each step of the modulation cycle, thereby reducing the effective coupling strength.

B. Propagation dynamics

Next we consider numerical simulations of the propagation dynamics to study the MI beyond the linear perturbation approximation. We take as the initial state the $k = 0$ Bloch wave plus a small random perturbation, i.e.,

$$|\psi(r, z = 0)\rangle = \frac{1}{\sqrt{2}}[1 + W p_a(r), 1 + W p_b(r)]^T, \quad (18)$$

where W is the relative strength of the random perturbation and the amplitude and phase of the complex perturbing amplitudes at each site $p_{a,b}(r)$ are sampled uniformly from the intervals $[0,1]$ and $[0,2\pi]$, respectively. The role of the random perturbation is both to mimic the imperfect excitation conditions which would be present in an experiment and to seed any instabilities so the instability modes grow to a significant amplitude within the considered propagation distance (50 modulation cycles). $W = 0.1$ is chosen as a trade-off between having the instability develop sufficiently fast and avoiding a strong excitation of the other band.

Using this initial condition we solve the nonlinear Schrödinger Eq. (1) numerically using the split step method, periodic boundary conditions, and saturable nonlinearity. We average observables over 100 realizations of the initial random perturbation. To depict the findings of dynamical simulations, in this section we have chosen the nonlinearity parameter $|g| = 0.35$, for which the initial state is linearly unstable in all cases, with g negative in the CI and AFHOTI phases and positive in the TI and AFI phases.

To examine the propagation mode dynamics, we follow the evolution of the normalized real-space participation number P_r, the normalized Fourier space participation number P_k, the interband mixing strength, and the purity gap, whose dynamics are shown in Fig. 6.

The real-space participation number $P_r(z)$ determines the fraction of strongly excited lattice sites during propagation. It is defined by the expression [25]

$$P_r = \frac{\mathcal{P}^2}{2N}\left(\sum_r |a_r|^4 + |b_r|^4\right)^{-1}, \quad (19)$$

where $\mathcal{P} = \sum_r \langle \psi(r)|\psi(r)\rangle$ is the total mode power and $N = 32 \times 32$ is the number of unit cells in the lattice, such that $0 \leqslant P_r \leqslant 1$.

The Fourier space participation number P_k is the k-space equivalent of P_r,

$$P_k = \frac{\mathcal{P}^2}{2N}\left(\sum_k |a_k|^4 + |b_k|^4\right)^{-1}, \quad (20)$$

which measures the fraction of excited Fourier modes. Averages of $P_r(z)$ and $P_k(z)$ over the ensemble of initial conditions are plotted in Figs. 6(a) and 6(b), respectively, for the CI, AFI, and AFHOTI phases.

To obtain the information on the efficiency of band mixing triggered by nonlinearity, we compute the fraction of energy
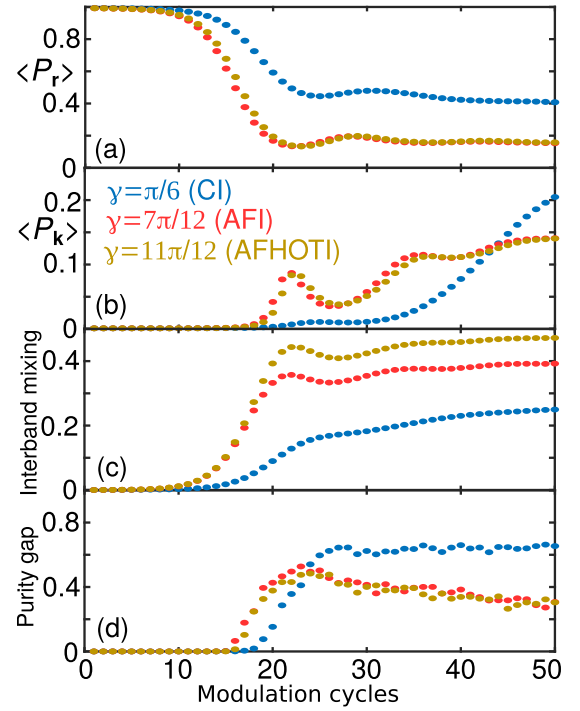

FIG. 6. Examples of MI instability dynamics in the nontrivial Floquet phases. (a) The real space participation number, indicating self-focusing from the initial uniform beam. (b) The Fourier space participation number, indicating spreading in k space. (c) The fraction of energy transferred from the initially excited band, indicating that more energy remains in the initial band. (d) The purity gap, indicating the emergence of a well-defined polarization state throughout the entire Brillouin zone.

transferred from the initially excited band to the rest of the system. This is carried out by projecting the field profile at the end of each modulation cycle onto the basis of linear modes of the Floquet evolution operator $\hat{U}_L(k, Z)$. When this fraction remains less than 0.5, the system retains some memory of the Floquet band that was excited at $z = 0$. This is the case for all three phases considered, as shown in Fig. 6(c).

We also compute the polarization components of the evolved field using Eqs. (8)–(11). When the polarization components are averaged over the ensemble of random initial perturbations we obtain mixed polarization states with purity $s^2 = s(k) \cdot s(k) < 1$. The purity gap $\min_k(s^2)$ plays a role analogous to the band gap of the linear lattice [34–36]; when the purity gap vanishes, there is at least one wave vector for which the polarization state is fully mixed, making the Chern number inferred from the polarization azimuth ill-defined. Figure 6(d) illustrates the dynamics of the purity gap, illustrating the emergence of a nonzero purity gap via the MI in all three phases.

Thus, even though the system is periodically driven (nonequilibrium), the MI is able to generate a quasi-steady-state in which P_r, the band populations, and the purity gap converge to (approximately) time-independent values. On the other hand, P_k maintains a slow growth, indicating that some memory of the initial state remains and an equilibrium state has not been reached yet. The simulations establish that slowly
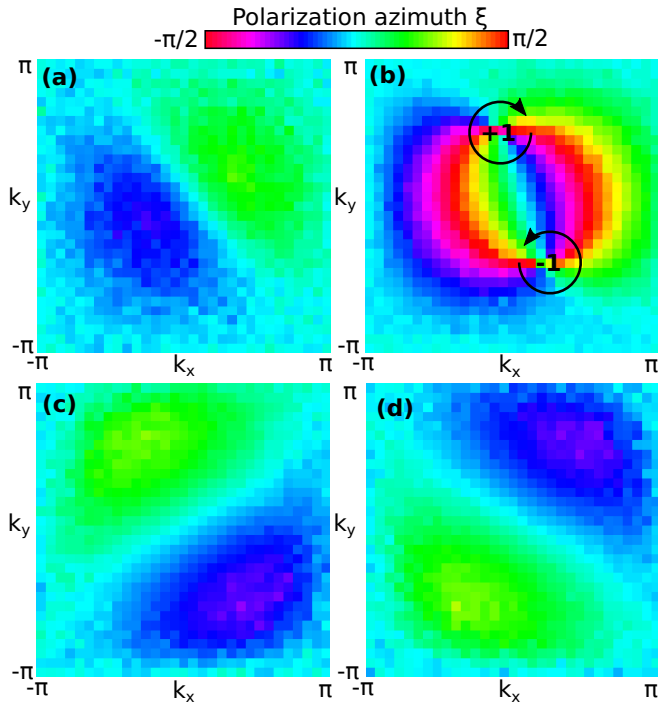
FIG. 7. Field polarization profiles in Fourier space, averaged over 100 random initial perturbations in the three phases. (a) Trivial insulator phase ($\gamma = \pi/24$). (b) Chern insulator phase ($\gamma = \pi/6$; ± 1 denotes the sign of the polarization ellipticity at the vortex cores. (c) Anomalous Floquet insulator phase ($\gamma = 7\pi/12$). (d) Anomalous Floquet higher order topological insulator phase ($\gamma = 11\pi/12$). The nonlinearity strength is $|g| = 0.35$ in all cases.

driven Floquet systems can exhibit similar relaxation dynamics, which is triggered by the nonlinear wave mixing, to this in the static topological lattices previously considered in Ref. [25].

Figure 7 shows the beam polarization profile in the quasisteady state (i.e., after 50 modulation cycles) in each of the topological phases. The qualitative features observed in the evolved beam's polarization textures match those obtained for the band's Bloch functions in Fig. 2. Vortices in the polarization profile can be created or destroyed in pairs at band crossing points, accompanied by the purity vanishing locally. The weighted sum of polarization vortex charge yields the Chern number. In Fig. 7, we verify that the Chern number is indeed nonzero in the CI phase, while it vanishes in the anomalous Floquet phases, since no polarization vortices occur in the quasisteady state.

Finally, Fig. 8 illustrates the beam measures as a function of γ, indicating the robustness of this quasi-steady-state provided the Floquet band gap remains open and the initial nonlinear Bloch wave is linearly unstable.

In summary, we have seen that the modulational instability of unstable nonlinear Bloch waves enables the complete population of a Floquet quasienergy band starting from a single wave vector, at least for sufficiently weak nonlinearity strengths. By measuring the polarization of the field after the instability has developed, we can obtain the Bloch wave's **k**-dependent polarization profile and thereby the band Chern
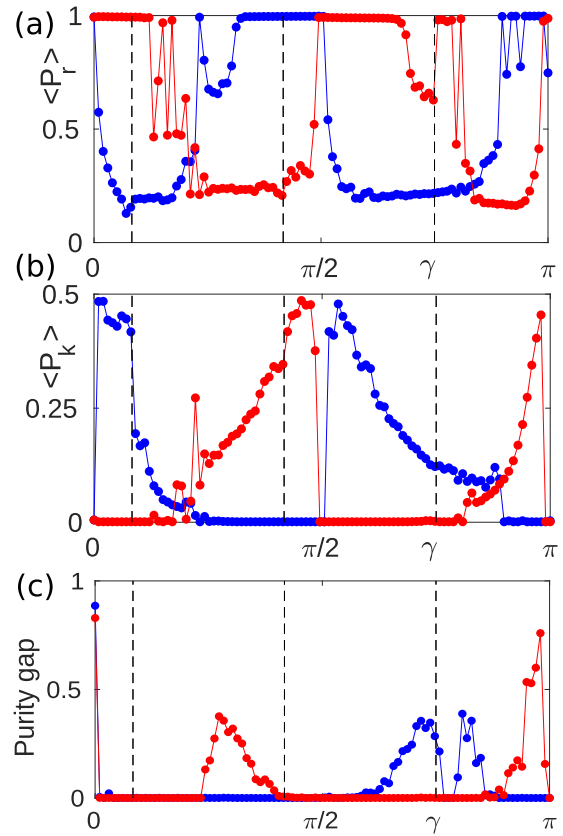

FIG. 8. The field measures after 50 modulation cycles as a function of γ for positive (blue) and negative (red) nonlinearity coefficients $|g| = 0.35$. Vertical dashed lines indicate the phase transitions. (a) Real-space participation number. (b) Fourier space participation number. (c) Purity gap. The purity gap vanishes in the vicinity of the phase transition points and over the range of γ where the nonlinear Bloch wave is linearly stable.

number, similar to the static lattice case considered previously in Ref. [25]. On the other hand, the anomalous Floquet phases, which cannot be distinguished using the Chern number, exhibit singularity-free polarization fields resembling that of the TI phase.

IV. MEASURING ANOMALOUS FLOQUET TOPOLOGICAL PROPERTIES

Next, we consider the identification of the anomalous Floquet topological phases using the nonlinear propagation dynamics. As noted in Sec. II, the anomalous Floquet topological invariants cannot be obtained by considering the eigenstates of the Floquet evolution operator $\hat{U}(Z)$. Instead, it is necessary to consider the dynamics during the entire driving period, e.g., by considering the phase bands of $\hat{U}(z)$. Unfortunately, the population of a single band of Floquet eigenstates via the modulational instability does not imply population of a single phase band, whose eigenstates can be strongly z-dependent. Therefore, one cannot straightforwardly distinguish the anomalous Floquet phases just by measuring the intracycle dynamics of the polarization in the steady state.

One might ask whether it is possible to excite only a single phase band by increasing the modulation period Z, such that

the phase bands undergo an adiabatic modulation. However, the phases we are interested in distinguishing are anomalous Floquet phases, which implies they do not have an adiabatic modulation limit; one inevitably encounters phase band crossing points during the modulation period, meaning that it is not possible to excite only a single phase band. Therefore, we need to take a different approach.

Our solution is to exploit the symmetry of the model. First, as we have shown in previous sections and which is fully consistent with Ref. [29], the anomalous Floquet phases can be distinguished by considering the properties of the phase bands only at the high-symmetry points of the Brillouin zone k_0. At these points, the phase-band eigenstates are independent of z; all that changes is the ordering of their eigenvalues, which become degenerate at z values corresponding to band crossing points z_m. At z_m, whatever initial polarization state there was at $z = 0$ will be restored, i.e., the evolution operator $\hat{U}(k_0, z_m) = \pm \hat{I}$. By tracking how the polarization rotates in the vicinity of the phase-band crossing points, we can extract the instantaneous Hamiltonian parameters and thereby the effective Hamiltonian Eq. (15), which can distinguish the different anomalous phases according to the scheme of Ref. [29].

Figure 9 illustrates the outlined approach for Γ point. First, we recall that from the dynamic equations for a nonlinear coupler with a coupling strength J,

$$i\partial_z \begin{pmatrix} a_r \\ b_r \end{pmatrix} = \begin{pmatrix} g|a_r|^2 & J \\ J & g|b_r|^2 \end{pmatrix} \begin{pmatrix} a_r \\ b_r \end{pmatrix}, \quad (21)$$

one can obtain a system of evolution equations for the spin components defined in real space, $s = \langle \psi_r | \hat{\sigma} | \psi_r \rangle$:

$$\partial_z s_z = 2J s_y, \quad (22a)$$

$$\partial_z s_y = -s_z(2J - g s_x), \quad (22b)$$

$$\partial_z s_x = -g s_y s_z, \quad (22c)$$

and conservation laws for the total intensity and spin

$$|a_r|^2 + |b_r|^2 = \text{const}, \quad (23a)$$

$$s_z^2 + s_y^2 + s_x^2 = \text{const}. \quad (23b)$$

We consider evolution of the initial state $(0, 1)^T$, which is a superposition of the symmetric (S) and antisymmetric (A) eigenstates. Being analogous to Fig. 4(d), Figure 9(a) shows behavior of the phase bands $\varphi_{S,A}(z)$ over the period Z in the linear case, $g = 0$. Assume we gradually cut out slices of the Floquet lattice sample from its end to find empirically, i.e., from polarization measurements, a position z_m, where the initial spin is restored $s_z(z_m) = s_z(0) = -1$ and a phase difference vanishes $\Delta\varphi(z_m) = \varphi_A(z_m) - \varphi_S(z_m) = 0$ [see Figs. 9(b) and 9(c)]. Next, we increase the intensity and at this fixed output coordinate z_m measure the spin.

We rewrite the phase difference $\Delta\varphi(z)$ in terms of the spins as $\Delta\varphi = \tan^{-1}(s_y/s_z)$. In the nonlinear regime $g \neq 0$, the phase difference becomes sensitive to the nonlinearity strength, as shown in Fig. 9(c), obeying the equation

$$\partial_z \Delta\varphi = -2J + g \frac{s_x s_z^2}{s_y^2 + s_z^2} = -2J + g \frac{s_x s_z^2}{1 - s_x^2}. \quad (24)$$

In Fig. 9(b), we mark the coordinate z_0, where $\Delta\varphi(z = z_0) = 0$ and, therefore, $s_y(z_0) = 0$, whereas $s_{z,x}$ exhibit minima. The
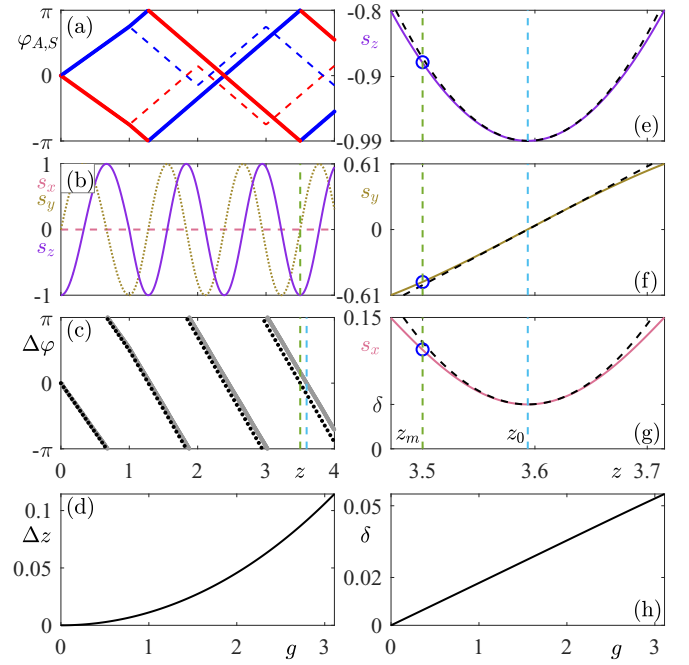

FIG. 9. (a) Phase bands $\varphi_A(z)$ (antisymmetric, red solid line) and $\varphi_S(z)$ (symmetric, blue solid line) at Γ point for $\gamma = 0.9\pi$, $\theta = 3\pi/4$ in the linear regime at $g = 0$. For comparison, phase bands $\varphi_{A,S}(z)$ at M point are shown with dashed lines. (b) Evolution of the spin components in the nonlinear regime over the whole period (solid line s_z, dotted line s_y, dashed line s_x). (c) Phase difference $\Delta\varphi = \varphi_A - \varphi_S$ in the linear case (black dotted line, $g = 0$) and $\Delta\varphi = \tan^{-1} s_y/s_z$ in the nonlinear case (gray solid line, $g = 0.9\pi$). The vertical green dashed line marks the coordinate z_m, at which measurements are taken, $s_x(z_m) = 0.112$, $s_z(z_m) = -0.86587$, $s_y(z_m) = -0.48756$; the vertical cyan dashed line marks the point z_0, where $s_y(z_0) = 0$ in the nonlinear case. (e)–(g) Evolution of the spin components in the nonlinear case in the vicinity of z_0: Blue lines are numerically obtained solutions, dashed black lines are their approximations Eqs. (26). Dependencies of the nonlinear shift $\Delta z = |z_m - z_0|$ (d) and $\delta = s_x(z_0)$ (h) on the nonlinearity strength g.

total spin conservation law at this point reads $s_{x0}^2 + s_{z0}^2 = 1$. We assume that nonlinearity is relatively weak and the nonlinear shift of z_0 with respect to z_m is small. Therefore, at z_0 we may approximately write

$$s_{x0} = \delta, \quad s_{z0} = -1 + \delta^2/2, \quad (25)$$

where $\delta \ll 1$ is a small parameter. In the vicinity of point z_0, we approximate the coordinate dependencies of the spin components as follows:

$$s_z = -1 + \frac{\delta^2}{2} + 2J^2(z - z_0)^2, \quad (26a)$$

$$s_x = \delta + gJ(z - z_0)^2, \quad (26b)$$

$$s_y = (2J - g\delta)(z - z_0), \quad (26c)$$

where J is the (unknown) coupling strength. Here, the deviations $|z - z_0|$ and $|\delta|$ are of the same smallness, both being caused by the presence of nonlinearity. To validate expressions Eqs. (26), we substitute Eqs. (26) into Eqs. (22) and (23b), and ensure they are consistently fulfilled in the zero
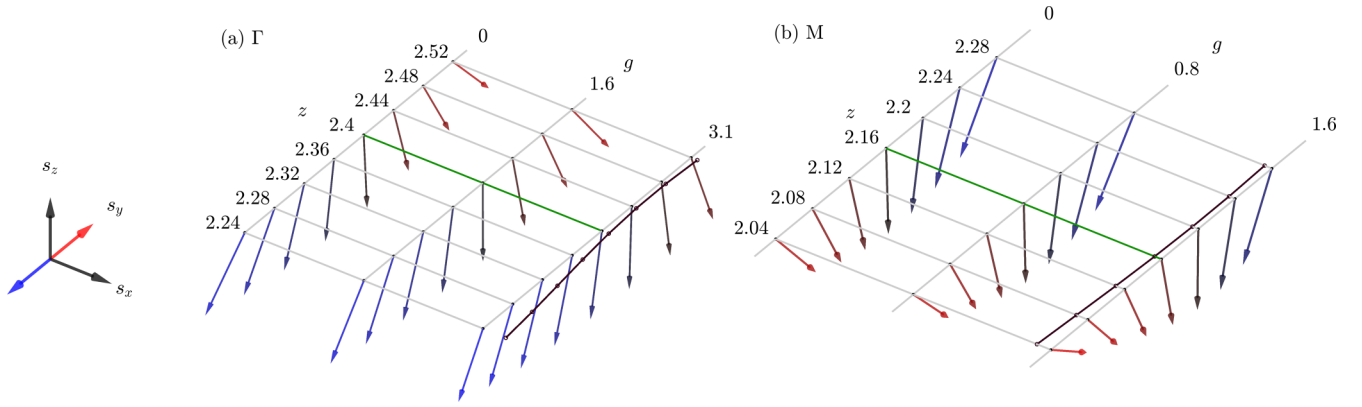
FIG. 10. Spin distribution $s = (s_x, s_y, s_z)$ in the vicinity of the coordinate z_m, where $\Delta\varphi(z = z_m)$ vanishes and the initial spin state $s(z = z_m) = s(z = 0) = (0, 0, -1)$ is restored in the linear ($g = 0$) case, for different nonlinearity strengths g. Arrow plots in panels (a) at Γ, and (b) at M, correspond to the middle crossing points in Fig. 9(a) with coordinates $z_m = 2.389$ and $z_m = 2.167$ (traced by green lines), respectively. The red (blue) color encodes the positive (negative) value of the s_y component, which has opposite trends in (a) $s_y = 2\gamma\Delta z_m$, and (b) $s_y = -2\gamma\Delta z_m$. The black line with dots visualises nonzero s_x at $g \neq 0$ in the third g slice. Parameters are $\theta = 3\pi/4$, $\gamma = 0.9\pi$.

δ^0 and first δ^1 orders of perturbation theory. In the linear limit, the spin s_x should be precisely equal to zero, thus, we anticipate two asymptotics $\delta = G_0 g$, $z_m - z_0 = G_1 g^2$, which are confirmed by Figs. 9(d) and 9(h). Taking a measurement of $s_x(z_m, g \to 0) \approx G_0 g$ at very small but non-negligible intensity, the coefficient G_0 may be determined. Then, performing a series of measurements for larger nonlinearity strengths g (or, equivalently, increasing the intensity of the incident light beam), we can obtain J from the system Eqs. (26).

Thus, the linear dependence of $s_y = 2J\Delta z_m$ in the vicinity of the phase band crossing points can be used to obtain the coupling strength, and thereby the sign characteristics of $\hat{H}_{\text{eff}}(\boldsymbol{k}_0, z)$ outlined in Table I, and distinguish the anomalous Floquet phases from the trivial phase, as discussed in Sec. II. Similarly, the described procedure can be used to characterize the crossing points in M direction. The spin behavior at the high-symmetry points is exemplified in Fig. 10. The arrow map illustrates the output polarization as a function of the nonlinearity for a lattice terminated such that a crossing of the phase bands occurs close to the linear limit, i.e., in the vicinity of the coordinate z_m, where the input superposition (s_z-polarized) state gets restored at $g = 0$. Specifically, we consider the middle crossing points within the third quarter of the period in Fig. 9(a). In the vicinity of z_m, the dependence of s_y on z and g is opposite at the Γ and M points, in agreement with the inversion symmetry eigenvalues in phase band diagrams of Fig. 4(d).

We note, however, that according to our calculations and Ref. [29], the approach based on the symmetry eigenvalues is still unable to distinguish the AFI phase from the AFHOTI phase.

V. CONCLUSION

Periodically driven lattices can host a wealth of different topological insulator phases, including CIs, AFIs, and their higher order analogs. The bulk-edge correspondence originates from the intrinsic relation between the bulk topological properties and the occurrence of topologically protected edge modes. Bulk topological invariants describing anomalous

Floquet phases generally depend on the details of the microevolution of the system, and have attracted a lot of interest over the past decade.

However, the observation and measurement of topological properties in experiments with driven systems is not a fully closed story. Following our earlier study Ref. [25], showing how nonlinear modulational instability in undriven topological lattices can be used to measure their bulk topological invariants, we tested the applicability of this approach to driven systems. The crucial findings of our study can be summarized in a few statements:

(1) For weak nonlinearity and gapped Floquet bands, the modulational instability is able to predominantly populate a single band starting from a single Bloch wave, enabling measurement of its Chern number via the polarization profile of the state generated by the modulational instability.

(2) To unveil topological properties of anomalous Floquet phases, it is generally necessary to consider the microscopic dynamics of the polarization field within the modulation cycle, which is challenging because the microscopic dynamics generally do not involve predominant excitation of a single band of the evolution operator $\hat{U}_L(z)$.

(3) In the special case of Floquet lattices with chiral symmetry, anomalous Floquet phases can be distinguished from the trivial phase by studying the time or nonlinearity-dependent dynamics of superpositions of Bloch waves at the high-symmetry points of the Brillouin zones.

Our methods can be readily implemented using light propagation in nonlinear waveguide arrays, similar to the experiments of Refs. [21–23], demonstrating the feasibility of using the nonlinear propagation dynamics to measure bulk topological invariants of energy bands.

ACKNOWLEDGMENTS

[1] T. Kitagawa, E. Berg, M. Rudner, and E. Demler, Topological chatacterization of periodically driven quantum systems, Phys. Rev. B **82**, 235114 (2010).

[2] N. Goldman and J. Dalibard, Periodically Driven Quantum Systems: Effective Hamiltonians and Engineered Gauge Fields, Phys. Rev. X **4**, 031027 (2014).

[3] A. Quelle, C. Weitenberg, K. Sengstock, and C. Morais Smith, Driving protocols for a Floquet topological phase without static counterpart, New J. Phys. **19**, 113010 (2017).

[4] M. S. Rudner, N. H. Lindner, E. Berg, and M. Levin, Anomalous Edge States and the Bulk-Edge Correspondence for Periodically Driven Two-Dimensional Systems, Phys. Rev. X **3**, 031005 (2013).

[5] G. M. Graf and C. Tauber, Bulk-edge correspondence for two-dimensional floquet topological insulators, Ann. Henri Poincaré **19**, 709 (2018)

[6] V. Dal Lago, M. Atala, and L. E. F. Foa Torres, Floquet topological transitions in a driven one-dimensional topological insulator, Phys. Rev. A **92**, 023624 (2015).

[7] F. Harper, R. Roy, M. S. Rudner, and S. L. Sondhi, Topology and broken symmetry in Floquet systems, Ann. Rev. Cond. Matt. Phys. **11**, 345 (2020).

[8] M. S. Rudner and N. H. Lindner, Band structure engineering and non-equilibrium dynamics in Floquet topological insulators, Nat. Rev. Phys. **2**, 229 (2020).

[9] L. Lu, J. D. Joannopoulos, and M. Soljacic, Topological photonics, Nature Photon. **8**, 821 (2014).

[10] T. Ozawa, H. M. Price, A. Amo, N. Goldman, M. Hafezi, L. Lu, M. C. Rechtsman, D. Schuster, J. Simon, O. Zilberberg, and I. Carusotto, Topological photonics, Rev. Mod. Phys. **91**, 015006 (2019).

[11] M. Kremer, L. J. Maczewsky, M. Heinrich, and A. Szameit, Topological effects in integrated photonic waveguide structures, Opt. Mat. Exp. **11**, 1014 (2021).

[12] D. Leykam, M. C. Rechtsman, and Y. D. Chong, Anomalous Topological Phases and Unpaired Dirac Cones in Photonic Floquet Topological Insulators, Phys. Rev. Lett. **117**, 013902 (2016).

[13] M. C. Rechtsman, J. M. Zeuner, Y. Plotnik, Y. Lumer, D. Podolsky, F. Dreisow, S. Nolte, M. Segev, and A. Szameit, Photonic Floquet topologicalinsulators, Nature (London) **496**, 196 (2013).

[14] L. J. Maczewsky, J. M. Zeuner, S. Nolte, and A. Szameit, Observation of photonic anomalous Floquet topological insulators, Nat. Commun. **8**, 13756 (2017).

[15] S. Mukherjee, A. Spracklen, M. Valiente, E. Andersson, P. Öhberg, N. Goldman, and R. R. Thomson, Experimental observation of anomalous topological edge modes in a slowly driven photonic lattice, Nat. Commun. **8**, 13918 (2017).

[16] S. Afzal, T. J. Zimmerling, Y. Ren, D. Perron, and V. Van, Realization of Anomalous Floquet Insulators in Strongly Coupled Nanophotonic Lattices, Phys. Rev. Lett. **124**, 253601 (2020).

[17] D. Smirnova, D. Leykam, Y. D. Chong, and Y. Kivshar, Nonlinear topological photonics, Appl. Phys. Rev. **7**, 021306 (2020).

[18] Y. Lumer, Y. Plotnik, M. C. Rechtsman, and M. Segev, Self-Localized States in Photonic Topological Insulators, Phys. Rev. Lett. **111**, 243905 (2013).

[19] Y. Lumer, M. C. Rechtsman, Y. Plotnik, and M. Segev, Instability of bosonic topological edge states in the presence of interactions, Phys. Rev. A **94**, 021801(R) (2016).

[20] D. Leykam and Y. D. Chong, Edge Solitons in Nonlinear Photonic Topological Insulators, Phys. Rev. Lett. **117**, 143901 (2016).

[21] S. Mukherjee and M. C. Rechtsman, Observation of Floquet solitons in a topological bandgap, Science **368**, 856 (2020).

[22] L. J. Maczewsky, M. Heinrich, M. Kremer, S. K. Ivanov, M. Ehrhardt, F. Martinez, Y. V. Kartashov, V. V. Konotop, L. Torner, D. Bauer, and A. Szameit, Nonlinearity-induced photonic topological insulator, Science **370**, 701 (2020).

[23] S. Mukherjee and M. C. Rechtsman, Observation of Unidirectional Soliton-Like Edge States in Nonlinear Floquet Topological Insulators, Phys. Rev. X **11**, 041057 (2021).

[24] M. Jürgensen, S. Mukherjee, M. C. Rechtsman, Quantized nonlinear Thouless pumping, Nature (London) **596**, 63 (2021).

[25] D. Leykam, E. Smolina, A. Maluckov, S. Flach, and D. A. Smirnova, Probing Band Topology using Modulational Instability, Phys. Rev. Lett. **126**, 073901 (2021).

[26] V. E. Zakharov and L. A. Ostrovsky, Modulation instability: The beginning, Physica D **238**, 540 (2009).

[27] R. W. Boyd, *Nonlinear Optics* (Academic Press, Oxford, 2008).

[28] T. Fösel, V. Peano and F. Marquardt, L lines, C points and Chern numbers: Understanding band structure topology using polarization fields, New J. Phys. **19**, 115013 (2017).

[29] W. Zhu, Y. Chong, and J. Gong, Symmetry analysis of anomalous Floquet topological phases, Phys. Rev. B **104**, L020302 (2021).

[30] W. Zhu, Y. D. Chong, and J. Gong, Floquet higher-order topological insulator in a periodically driven bipartite lattice, Phys. Rev. B **103**, L041402 (2021).

[31] F. Nathan and M. S. Rudner, Topological singularities and the general classification of Floquet-Bloch systems, New J. Phys. **17**, 125014 (2015).

[32] M. Holthaus, Floquet engineering with quasienergy bands of periodically driven optical field, J. Phys. B **49**, 013001 (2016).

[33] S. M. Jensen, The nonlinear coherent coupler, IEEE J. Quantum Electron. **18**, 1580 (1982).

[34] Y. Hu, P. Zoller, and J. C. Budich, Dynamical Buildup of a Quantized Hall Response from Nontopological States, Phys. Rev. Lett. **117**, 126803 (2016).

[35] C.-E. Bardyn, M. A. Baranov, C. V. Kraus, E. Rico, A. İmamoğlu, P. Zoller, and S. Diehl, Topology by dissipation, New J. Phys. **15**, 085001 (2013).

[36] J. C. Budich and S. Diehl, Topology of density matrices, Phys. Rev. B **91**, 165140 (2015).